Influence of microstructural defects and the surface topography on the fatigue behavior of "additively-subtractively" manufactured specimens made of AISI 316L

Einfluss mikrostruktureller Defekte und der Oberflächentopographie auf das Ermüdungsverhalten „additiv-subtraktiv" gefertigter Proben aus AISI 316L

B. Blinn[1], S. Greco[2], M. Smaga[1], M. Zimmermann[2], H. Hotz[2], D. Müller[2], J. Hartig[2], B. Kirsch[2], J.C. Aurich[2], T. Beck[1]

As additive manufacturing offers only low surface quality, a subsequent machining of functional and highly loaded areas is required. Thus, a sound knowledge of the interrelation between the additive and subtractive manufacturing process as well as the resulting mechanical properties is indispensable. In this work, specimens were manufactured by using laser-based powder bed fusion (L-PBF) with substantially different sets of process parameters as well as subsequent grinding (G) or milling (M). Despite the substantially different surface topographies, the fatigue tests revealed only a slight influence of the subtractive manufacturing on the fatigue behavior, whereas the different laser-based powder bed fusion process parameters led to pronounced changes in fatigue strength. In contrast, a significant influence of subtractive finishing on the fatigue properties of the defect-free continuously cast (CC) reference specimens was observed. This can be explained by a dominating influence of process-induced defects in laser-based powder bed fusion material, which overruled the influence of surface machining. However, although both laser-based powder bed fusion parameter sets resulted in substantial defects, one set yielded similar fatigue strength compared to continuously cast specimens.

Keywords: Laser-based powder bed fusion / process-induced defects / subtractive manufacturing / fatigue behavior / AISI 316L

Da die additive Fertigung zu einer geringen Oberflächengüte führt, ist eine spanende Nachbearbeitung von hochbeanspruchten Bereichen oder Funktionsflächen notwendig, weshalb ein Verständnis der Wechselwirkung zwischen additiver und subtraktiver Fertigung und den hieraus resultierenden mechanischen Eigenschaften unabdingbar ist. In dieser Arbeit wurden Proben mittels laserbasiertem Pulverbettschmelzen (L-PBF), unter Verwendung zweier substantiell unterschiedli-

[1] TU Kaiserslautern, Institute of Materials Science and Engineering (WKK), Gottlieb-Daimler-Straße 44, 67663, KAISERSLAUTERN, GERMANY
[2] TU Kaiserslautern, Institute for Manufacturing Technology and Productions Systems (FBK), Gottlieb-Daimler-Straße 44, 67663, KAISERSLAUTERN, GERMANY

Corresponding author: B. Blinn, TU Kaiserslautern, Institute of Materials Science and Engineering (WKK), Gottlieb-Daimler-Straße 44, 67663, KAISERSLAUTERN, GERMANY,
E-Mail: blinn@mv.uni-kl.de

cher Parametersätze, sowie nachgelagertem Schleifen (G) bzw. Fräsen (M) hergestellt. Trotz der unterschiedlichen Oberflächentopographien zeigten die Ermüdungsversuche nur einen geringen Einfluss der Nachbearbeitung auf die Ermüdungslebensdauer, während die verschiedenen, im laserbasierten Pulverbettschmelzen verwendeten Prozessparameter zu deutlich anderen Ermüdungsfestigkeiten führten. Für die stranggegossenen, defektfreien Referenzproben (CC) wurden hingegen erhebliche Auswirkungen der Nachbearbeitung auf das Ermüdungsverhalten beobachtet. Dies kann auf den dominierenden Einfluss prozessinduzierter Defekte bei den mittels laserbasierten Pulverbettschmelzen hergestellten Proben zurückgeführt werden. Trotz der Defekte war jedoch für einen dieser Zustände eine zu den stranggegossenen, defektfreien Referenzproben vergleichbare Ermüdungsfestigkeit festzustellen.

Schlüsselwörter: Laserbasiertes Pulverbettschmelzen / prozessinduzierte Defekte / subtraktive Nachbearbeitung / Ermüdungsverhalten / AISI 316L

1 Introduction

Additive manufacturing processes are increasingly applied in industry, which is mainly driven by the possibility to manufacture prototypes and small batches rapidly and cost-efficiently and that additive manufacturing provides a high degree of freedom in design [1, 2]. For the production of metal components with complex geometries and filigree structures, laser-based powder bed fusion (L-PBF) processes are commonly used. In these processes, the component is manufactured layer-by-layer from a metal powder bed [3]. The powder within the layer of the later component is locally melted by a laser. When cooling down to ambient temperature, the material re-solidifies, resulting in a metallurgical bond with the underlying material. Subsequently, the building platform is lowered by the value of the layer thickness and the next powder layer is applied and melted. This process is repeated until the component is completed [4].

This manufacturing process results in a complex, unique and fine-grained microstructure, which exhibits grains elongated along the build-up direction, caused by the heat flux into the already solidified material [5–8]. These grains grow beyond the melt pool boundaries and contain cellular dislocation structures due to the relatively high cooling rates [5, 6, 8, 9].

The metallurgical and mechanical properties of the resulting materials significantly depend on the manufacturing parameters used. An excessively high laser power in laser-based powder bed fusion process can cause evaporation of the material, which leads to a high porosity [10]. To consider the relation between the most influencing manufacturing parameters, i.e., laser power P_L, scanning velocity v_s, hatching distance d and layer thickness t, the value of volume energy density E_{vol}, which can be determined with equation (1), is commonly used [8, 11–13]. With increasing volume energy density a decreasing porosity can be achieved [11, 13, 12]. However, by using too high volume energy density E_{vol} also an increased porosity can be observed [10, 11, 13].

$$\mathrm{E_{vol}} = \frac{\mathrm{P_L}}{\mathrm{v_s \cdot d \cdot t}} \tag{1}$$

Parts produced with laser-based powder bed fusion usually have a poor surface quality and a low dimensional accuracy. Typical surface roughness values of parts in additively manufactured ("as-built") condition are in the range of $R_a = 29$ µm–41 µm ($R_z = 154$ µm–184 µm), which depends on the manufacturing parameters and the material used [14]. Common dimensional errors are between 0.01 %–34 % of the target values and also depend on the manufacturing parameters and material [15, 16].

The process-induced microstructural defects, i.e., pores and lack of fusion, lead to a significant reduction of the fatigue lifetime of additively manufactured materials [17–22]. Besides these process-induced defects, the relatively high surface roughness of additively manufactured materials results in

notch effects and thus, in a reduction of the fatigue strength (> 50 %) [7, 21, 23].

Consequently, subtractive manufacturing of critical and functional areas is a prerequisite to ensure the functionality and reliability of additively manufactured components. The most common post-processing technology that is used in combination with additive manufacturing is machining [24]. Thereby, grinding and milling are suitable subtractive processes to significantly reduce the surface roughness of additively manufactured structures [25–27].

Furthermore, additively manufactured materials exhibit relatively high residual stresses, which depend on the process parameters. The build-up direction has a significant impact on the residual stresses, which are further influenced by the geometry of the workpiece [7, 28, 29]. This unique residual stress state, combined with the specific microstructure of additively manufactured materials, results in differences in the machinability compared to conventionally manufactured materials. Consequently, differences in surface morphology, i. e., surface topography and properties (e. g. hardness, residual stresses, microstructure, etc.), were observed between finished additively manufactured components and identically finished reference parts [27, 30–32]. In conclusion, the interaction of additively manufactured materials with subtractive manufacturing differs from common materials of the same chemical composition, resulting in different surface morphologies. Note that such differences in surface layer have a substantial impact on the fatigue behavior of a material [33, 34].

As additive manufacturing offers a high potential to produce safety relevant structural components, where a sound knowledge of the cyclic properties is indispensable, the presented work focuses on the fatigue behavior of specimens manufactured by laser-based powder bed fusion. In accordance with preliminary own work, the commonly used austenitic stainless steel AISI 316L was utilized as investigated material [19–22, 26, 27, 35]. Because the "as-built" surface of additively manufactured parts leads to a dramatic decrease of fatigue strength and additive manufacturing only offers a low level of dimensional accuracy, subtractive manufacturing of additively manufactured parts is of great interest. Consequently, the interaction of additive and subtractive manufacturing processes and their influence on the cyclic properties of the material is analyzed in this work. Therefore, specimens with "as-built" (AB), milled (M) as well as ground (G) surfaces were investigated. In the following the expression "additively-subtractively" represents the combination of the additive manufacturing process (L-PBF) and a subsequent subtractive manufacturing (grinding; milling). Moreover, two sets of process parameters, which were determined in preliminary work, were utilized to realize substantially different conditions of the additively manufactured material [35]. As a reference for conventionally manufactured material, continuously cast (CC) specimens were also ground and milled. The fatigue behavior of the different conditions was analyzed by using fatigue tests, fatigue fracture surface investigation and measurement of the surface topography as well as residual stresses. By analyzing the cyclic properties, the influence of process-induced defects, surface roughness as well as the strength of the material volume are considered. Furthermore, the influence of the residual stresses, resulting from subtractive finishing, is taken into account.

2 Manufacturing processes

2.1 Additive manufacturing of fatigue specimens

The fatigue specimens were additively manufactured with laser-based powder bed fusion (L-PBF) by using a Mlab Cusing from Conceptlaser[1], *Figure 1*a. This system has an available building volume of 90 mm × 90 mm × 80 mm and is equipped with a neodymium-doped yttrium aluminum garnet (Nd:YAG) fiber laser with a wavelength of $\lambda =$ 1064 nm, a spot diameter of $\delta = 50$ µm as well as a maximum power of 100 W. For manufacturing, a nitrogen inert gas atmosphere was used for oxidation prevention and the building platform was not heated during the manufacturing process. Two sets of process parameters (L-PBF1 and L-PBF2) were used, which differ in scanning speed as well as laser power and hence, in E_{vol} ($\Delta E_{vol} = 85.7$ J/mm^3), to realize two substantially different material conditions, *Table 1*. These parameter sets were determined in preliminary work and ensure significant differences in porosity as well as surface roughness [35]. This enables the analysis of the interrelation between the process-induced material condition,

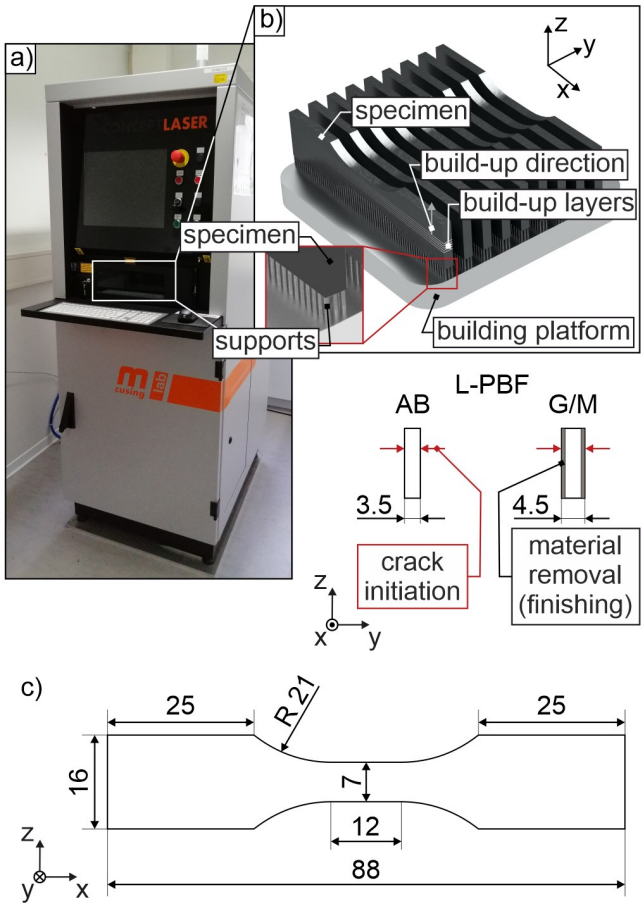

Figure 1. a) Laser-based powder bed fusion (L-PBF) system Mlab Cusing, b) positioning of the specimens on the building platform as well as c) geometry of the "as-built" (L-PBF-AB) and "additively-subtractively" manufactured (L-PBF-G/L-PBF-M) fatigue specimens.

Bild 1. a) Pulverbettanlage Mlab Cusing, b) Positionierung der Ermüdungsproben auf der Bauplattform sowie c) Geometrie der "as-built" (L-PBF-AB) und "additiv-subtraktiv" gefertigten (L-PBF-G/L-PBF-M) Ermüdungsproben.

surface roughness and resulting fatigue behavior as well as their interaction with subtractive manufacturing process. For both process parameter sets the successive chessboard pattern was chosen as scanning strategy.

The specimens were fixed on the building platform using cone-shaped supports with a diameter of 0.8 mm and heights from 4 mm to 8.5 mm. The supports were arranged in a rectangular pattern with 1.3 mm center-to-center distance in x- as well as y-direction. The positioning of the specimens on the building platform results in layer planes parallel to the loading direction in fatigue tests, Figure 1b.

The specimens with "as-built" (AB) surface were manufactured net-shape and thus, had a thickness of 3.5 mm after laser-based powder bed fusion, Figure 1. For the machined specimens a stock allowance is needed and therefore, these specimens had a thickness of 4.5 mm after laser-based powder bed fusion and were finished by grinding (G) or milling (M) to a thickness of 3.5 mm, Figure 1. The broad faces of the specimens (x-z-plane in Figure 1b and c) were machined as described in sections 2.2 and 2.3, while the small faces (x-y-plane in Figure 1b) were polished at all specimens (including the "as-built" condition). This led to significantly lower surface roughness as well as round edges on the small faces, which ensured fatigue crack initiation at the finished broad faces of the gauge length, Figure 1.

The circularity c of the used powder particles was determined according to [36] with equation (2), where A corresponds to the projected area of the individual powder particles and U to the circumference of this area. Higher values of c correspond to a higher level of circularity, whereby $c = 1$ represents an ideal circle.

$$c = \sqrt{\frac{4\pi \cdot A}{U^2}} \tag{2}$$

Table 1. Process parameters used in laser-based powder bed fusion.

Tabelle 1. Im laserbasierten Pulverbettschmelzen verwendete Prozessparameter.

Condition	Laser power [W]	Scanning speed [mms^{-1}]	Layer thickness [µm]	Hatching distance [µm]	E_{vol} [Jmm^{-3}]
L-PBF1	70	1,500	25	56	33.3
L-PBF2	50	300	25	56	119.0

Due to the high circularity of the powder particles (90 % of the particles > 0.93), the projected area of the powder particles was assumed to be equivalent to the area of a circle, *Figure 2*b. The equivalent diameters of the powder particles were used to determine the particle size distribution, Figure 2a. The weighted mean diameter d_{50}, which indicates that 50 % of all powder particles are smaller than this characteristic value, is 32 µm. Based on the same definition, the values $d_{10} = 20$ µm and $d_{90} = 45$ µm are additionally specified in order to describe the width of the particle size distribution.

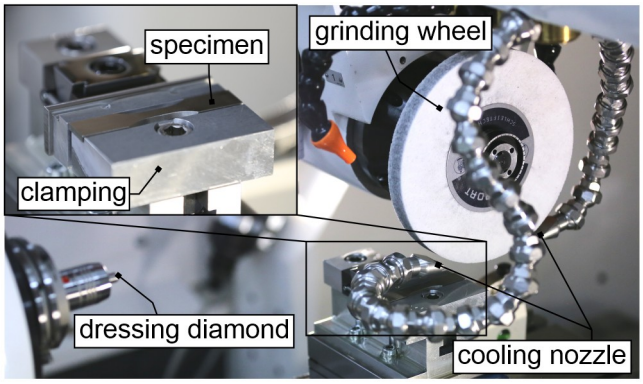

Figure 3. Experimental setup for pendulum grinding.

Bild 3. Experimenteller Aufbau des Pendelschleifprozesses.

2.2 Grinding

Pendulum surface grinding of the fatigue specimens was performed on a 5-axis CNC tool grinding machine of type Walter Helitronic Vision[1], *Figure 3*. The tool used was a conventional corundum (Al_2O_3; F80) 1 A1 grinding wheel (200 mm × 20 mm × 20 mm). Mineral oil was utilized as cooling lubricant and supplied with two nozzles, which had a flow rate of 30.5 l/min (jet exit velocity: 18 m/s), respectively. A grinding wheel speed of 30 m/s, a feed velocity of 15,000 mm/min and a depth of cut of 0.005 mm were used. The direction of feed motion of the grinding wheel corresponded to the longitudinal direction (x-direction in Figure 1c) of the fatigue specimens. In order to minimize distortion, ten passes were carried out alternately on each side. After grinding of each specimen, the grinding wheel was dressed with three passes using a fixed dressing diamond. Therefore, a grinding wheel speed of 30 m/s, a dressing depth of cut of 0.03 mm and an axial dressing feed rate of 200 mm/min were utilized.

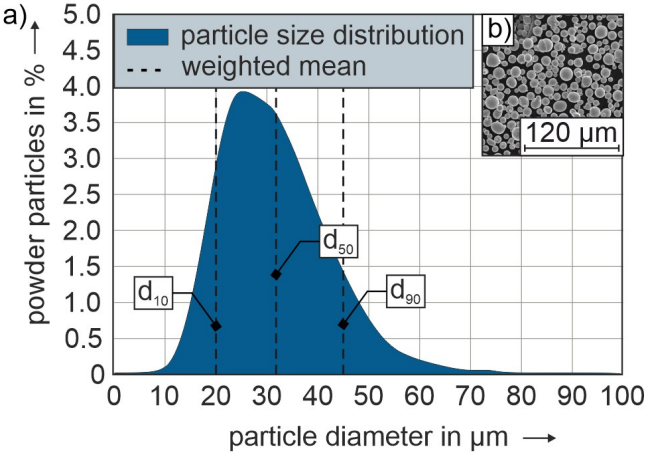

Figure 2. a) Particle size distribution and b) scanning electron microscope image of the used powder.

Bild 2. a) Partikelgrößenverteilung und b) rasterelektronenmikroskopische Aufnahme des verwendeten Pulvers.

2.3 Milling

Milling was performed on a 5-axis machining center (DMU 70 eVolution[1]), *Figure 4*. An inserted tooth cutter (type: R245-050Q22-12 M) with a diameter of 50 mm and four teeth was used. The indexable inserts (type: R245-12 T3 M-PL S30T) consisted of a cemented carbide substrate and a

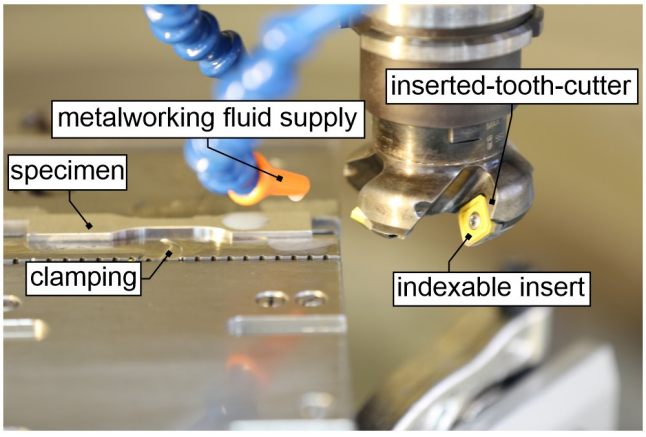

Figure 4. Experimental setup for milling.

Bild 4. Experimenteller Aufbau des Fräsprozesses.

$TiCN\text{-}Al_2O_3\text{-}TiN$ multilayer coating. For all milling operations a cutting speed of 94.2 m/min and a feed velocity of 150 mm/min were selected. The width of cut matched the width of the specimens and the metalworking fluid was supplied for cooling as well as lubrication during milling process. The direction of feed motion corresponded to the longitudinal direction of the fatigue specimens, Figure 1c (x-direction). In order to minimize distortion, a depth of cut of 50 µm was chosen and both sides of the fatigue specimens were milled alternately.

3 Characterization methods and materials

3.1 Characterization methods

The light optical micrographs in the presented work were taken with a Leica[1] DM 6000. For visualization of the grain structure and the layer boundaries, a V2A etchant was used. To examine the porosity of each material condition, light optical micrographs of cross sections as well as longitudinal sections of the clamping shafts of two specimens were analyzed, respectively. Note that the actual value of the porosity as well as the pore diameter can deviate from the measured values based on light optical micrographs, as three-dimensional objects are analyzed by using two-dimensional sections. However, this method is sufficient to compare the presented conditions.

To determine the surface roughness of the differently manufactured specimens, topography analyses were conducted with a nanofocus[1] µsurf Explorer confocal microscope with an object lens of type 800S (magnification: 20x; numerical aperture: 0.45). For each condition, the broad frontside and backside of four randomly chosen specimens were investigated by using 10 measuring fields (5 on frontside and 5 on backside) of 2.4 mm × 2.4 mm, respectively, Figure 1b, c (x-z-plane). Within the presented results no influence of measuring field position was observed and thus, all measurements were used to determine representative mean values of S_a and S_z in accordance with DIN EN ISO 25178-2 [37].

The macro hardness (HV30) was measured with a Zwick/Roell[1] ZHU250 tabletop device and the micro hardness (Martens hardness – *HM*) was characterized with a Fischerscope H100 C device of Helmut Fischer GmbH[1], which enables a precise localization of the indentation points and thus, the determination of the hardness in the solid areas of porous structures. The macro as well as micro hardness values for each condition are based on measurements on longitudinal and cross sections, prepared out of clapming shafts of a minimum number of two specimens. The hardness measurements revealed no influence of indentation direction in relation to build-up direction. While macro hardness was determined by using a minimum number of 6 measurements respectively, micro hardness values are based on a minimum number of 20 indentation points for each material (L-PBF1; L-PBF2; CC). The indentation force in micro indentation tests was 50 mN and the dwell time was 10 s.

To analyze the residual stresses in loading direction (x-direction in Figure 1c), x-ray diffraction measurements were carried out on the broad faces of the specimens (x-z-plane in Figure 1b, c), using copper potassium (Cu–K) α_1-radiation and a spot size of 3.0 mm × 3.0 mm. Therefore, an x-ray tube voltage of 40 kV, an x-ray tube current of 40 mA and a scanning speed of 0.004 °/s were utilized. The residual stresses were determined by means of the $\sin^2\psi$ method from diffraction peak at the (220) austenite lattice plane.

The fatigue tests were performed stress-controlled on a servo-hydraulic testing device of type Schenck[1] PSA16 with a stress ratio $R = -1$ and a frequency $f = 2$ Hz. The relatively low frequency was used to avoid extensive plastic deformation-induced self-heating of the specimens [19]. To achieve a feasible test duration with this frequency, the limit of number of cycles was defined as $2 \cdot 10^6$. To analyze the cyclic deformation behavior, the stress-strain hysteresis loops and hence, plastic strain amplitude $\varepsilon_{a,p}$, were determined by using a capacitive extensometer. Moreover, the magnetic fraction ζ in the gauge length of the specimens was measured before and after the fatigue tests with a FERITSCOPE™ MP 30E device of Helmut Fischer GmbH[1]. The increase of magnetic fraction $\Delta\zeta$ qualitatively represents the amount of transformation from paramagnetic austenite to ferromagnetic α'-martensite, resulting from cyclic deformation. In the presented investigations, the specimens manufactured by laser-based powder bed fusion revealed

no magnetic fraction in the gauge length before fatigue testing, whereas continuously cast specimens showed approximately 0.3 Fe-%. The low amount of magnetic fraction in continuously cast specimens is presumably caused by deformation-induced phase transformation during subtractive manufacturing, correlating with its lower austenite stability, *Table 2*.

For fatigue fracture surface analyses, a scanning electron microscope of type FEI[1] Quanta 600 was utilized. All fatigue specimens revealed fatigue crack initiation from the specimens' broad side, enabling the analysis of the influence of the different surface conditions on the fatigue behavior, Figure 1 (x-z-plane).

3.2 Materials

3.2.1 Volume material

To explore the interaction of additive and subtractive manufacturing processes as well as their influence on the fatigue behavior, different conditions of additively and "additively-subtractively" manufactured specimens were investigated, *Figure 5*. Therefore, two different parameter sets were used for laser-based powder bed fusion process and three different surface conditions were realized, respectively: i) no subtractive finishing ("as-built" (AB)), ii) ground (G) and iii) milled (M). As a reference for conventional manufacturing, continuously cast (CC) and subsequently milled specimens were investigated with ground as well as milled surface condition. In summary, eight different types of specimens were analyzed.

The chemical compositions of the materials produced with laser-based powder bed fusion and continuous casting were determined by spectrophotometry on the specimen clamping shafts, Table 2. For the investigated materials significant differences in chemical composition were observed, i. e., the additively manufactured material exhibits higher contents of nickel (2.2 wt.%), chromium (1.2 wt.%) and nitrogen (0.04 wt.%). However, both materials meet the limits of the ASTM standard [38].

The investigated AISI 316L can be metastable at ambient temperature, resulting in deformation-induced austenite-α'-martensite transformation at cyclic loading [19–21]. Consequently, the austenite stability, which mainly depends on the chemical

Table 2. Chemical composition and $M_{d30,\ Angel}$ of investigated materials.

Tabelle 2. Chemische Zusammensetzung und $M_{d30,\ Angel}$ der untersuchten Werkstoffe.

Alloying element [wt.%]	C	N	Si	Mn	Cr	Ni	Mo	Fe	$M_{d30,\ Angel}$ [°C]
L-PBF	0.02	0.10	0.68	1.35	18.0	12.5	2.34	64.9	−68.6
CC	0.03	0.06	0.37	1.34	16.8	10.3	2.02	68.3	−8.2
ASTM min [38]	–	–	–	–	16.0	10.0	2.00	60.8	61.8
ASTM max [38]	0.03	0.10	1.00	2.00	18.0	15.0	3.00	72.0	−117.1

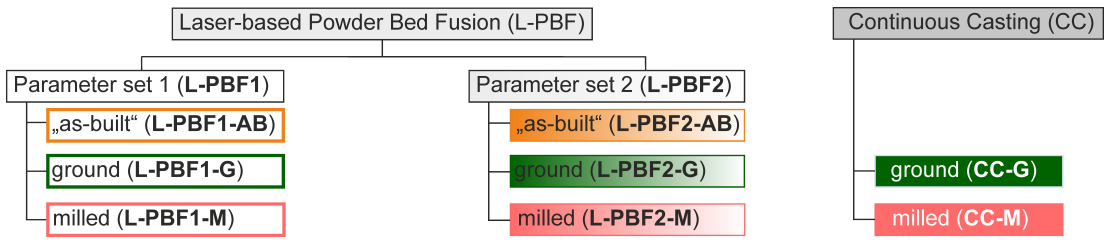

Figure 5. Overview of the investigated types of additively and conventionally manufactured specimens made of AISI 316L with different surface conditions.

Bild 5. Übersicht der untersuchten, aus AISI 316L additiv und konventionell gefertigten, Ermüdungsproben mit unterschiedlichen Oberflächenzuständen.

Table 3. Porosity, equivalent pore diameter and macro (HV30) as well as micro (HM) hardness of investigated materials.

Tabelle 3. Porosität, äquivalenter Porendurchmesser und Makro- (HV30) sowie Mikrohärte (HM) der untersuchten Werkstoffe.

Material	Porosity	Equivalent pore diameter		Hardness	
		average	maximum	macro	micro
	[area-%]	[µm]	[µm]	[HV30]	[GPa]
L-PBF1	17.41 ± 2.51	29.6 ± 4.3	252.3 ± 41.5	–	2.5 ± 0.17
L-PBF2	0.58 ± 0.55	11.5 ± 4.5	103.2 ± 56.1	222 ± 4	2.7 ± 0.13
CC	0.03 ± 0.01	4.5 ± 0.4	17.1 ± 5.0	176 ± 6	2.1 ± 0.06

composition, has to be considered. Therefore, for both materials M_{d30} was determined according to [39] with equation (3). M_{d30} is defined as the temperature that leads to a transformation of 50 % of the initial to α'-martensite at a plastic strain of 30 %. Higher M_{d30} represents lower austenite stability and thus, a higher amount of austenite-α'-martensite transformation is expected for CC specimens in the fatigue tests, Table 2.

$$M_{d30,\,Angel} = 413 - 462\,(\mathrm{C} + \mathrm{N}) - 9.2\,\mathrm{Si} - 8.1\,\mathrm{Mn} - 13.7\,\mathrm{Cr} - 9.5\,\mathrm{Ni} - 18.5\,\mathrm{Mo} \quad (3)$$

Due to significantly higher volume energy density E_{vol}, L-PBF2 results in lower porosity (−16.83 area-%) as well as smaller average (−18.1 µm) and maximum pore sizes (−149.1 µm) compared to L-PBF1, *Table 3*, *Figure 6*a, b. To examine the impact of laser-based powder bed fusion process parameters on porosity and surface roughness as well as their influence on the fatigue behavior, significantly different parameter sets were used, which were determined in preliminary work [35]. Although L-PBF1 yields high porosity, which is not representable for densities achievable with laser-based powder bed fusion (L-PBF), it enables an investigation of the interrelation of porosity and surface machining on the fatigue behavior. However, L-PBF2 represents a condition equivalent to the state of the art [19].

To analyze the influence of the laser-based powder bed fusion parameter sets on the mechanical properties, hardness measurements were conducted. As the porosity of the L-PBF1 specimens was too high to determine reliable macro hardness values,

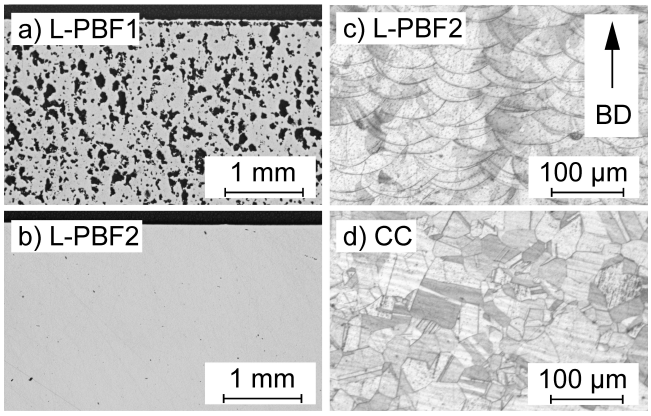

Figure 6. Light optical micrographs of porosity (a and b) and microstructure (c and d) of differently produced materials.

Bild 6. Lichtmikroskopische Aufnahmen der Porosität (a und b) sowie der Mikrostruktur (c und d) der unterschiedlich hergestellten Werkstoffe.

the Martens hardness (HM) was determined by using an indentation force of $F = 50$ mN. This enables the determination of the hardness of the material volume between the pores. Compared to L-PBF2, L-PBF1 leads to slightly lower hardness (92.6 %) of the material volume.

The conventionally manufactured material has a significantly lower macro (HV30; -79.3 %) as well as micro hardness (HM; −84.0 % and −77.8 %) in comparison to the materials produced with laser-based powder bed fusion, Table 3. This is caused by the higher cooling rates achieved with laser-based powder bed fusion, leading to a refined microstructure [19], Figure 6c, d. Moreover, the continuously cast material reveals a significantly lower level of porosity (−17.38 area-% and −0.55 area-

%) as well as average (−25.1 µm and −7.0 µm) and maximum pore sizes (−235.1 µm and −86.1 µm) compared to the specimens made by laser-based powder bed fusion.

The light optical micrographs show a fully austenitic microstructure of the differently manufactured materials, Figure 6c, d. Whereas L-PBF1 yields a high number of pores, L-PBF2 and Continuous Casting leads to a dense material volume and thus, enabling a microstructural analysis. The continuously cast material shows globular grains, while elongated grains along the build-up direction result from L-PBF2, Figure 6c, d. The grains in materials produced with L-PBF2 grow beyond the melt pool boundaries, which are visible in LOMs. The microstructure observed for additively manufactured material is characteristic and corresponds to [5–7, 19–22].

3.2.2 Surface conditions

Besides the properties of the material volume and the porosity, the different parameter sets in laser-based powder bed fusion process influence the surface topography of the specimens. Comparing the additively manufactured specimens in "as-built" condition, L-PBF1 leads to slightly lower S_a (−1.54 µm), but significantly higher S_z (68.98 µm) in relation to L-PBF-2, *Table 4*. Note that S_z is more important for the fatigue lifetime, because it represents the most critically geometrical surface-induced notch effect, which has to be considered by comparing the fatigue behavior of different surface conditions [40].

However, subsequent machining of the specimens manufactured by using L-PBF1 and L-PBF2 results in a substantial decrease of S_a (about −5 µm for L-PBF1 and −9 µm for L-PBF2) as well as S_z (more than −130 µm for L-PBF1 and more than −110 µm for L-PBF2), Table 4. In ground as well as milled condition the L-PBF2 specimens show lower S_a (−2.58 µm and −2.38 µm) and S_z (−47.41 µm and −18.22 µm) compared to L-PBF1, respectively. This can be explained by the significantly higher porosity resulting from L-PBF1, which increases the probability of exposed pores and hence, contributes to a higher surface roughness. Because of the greater S_z of L-PBF1 specimens, combined with their significantly higher porosity, a higher fatigue strength of L-PBF2 specimens is expected, Tables 3, 4.

Table 4. Surface roughness (S_a and S_z) of differently manufactured specimens.

Tabelle 4. Oberflächenrauigkeit (S_a and S_z) der unterschiedlich hergestellten Proben.

Condition	S_a [µm]	S_z [µm]
L-PBF1-AB	9.45 ± 0.50	197.63 ± 26.83
L-PBF1-G	4.56 ± 1.81	64.55 ± 15.95
L-PBF1-M	3.77 ± 0.61	28.03 ± 6.58
L-PBF2-AB	10.99 ± 1.27	128.65 ± 15.47
L-PBF2-G	1.98 ± 0.95	17.14 ± 4.15
L-PBF2-M	1.39 ± 0.47	9,81 ± 2.15
CC-G	5.30 ± 2.66	31.36 ± 12.77
CC-M	5.09 ± 0.61	25.88 ± 4.42

In ground and milled condition, the continuously cast material exhibits a significantly rougher surface, i.e., higher S_a (3.32 µm and 3.70 µm) and S_z (14.22 µm and 16.07 µm), than the machined L-PBF2 specimens. Moreover, machining of CC specimens yields slightly higher S_a compared to the machined L-PBF1 specimens (0.74 µm and 1.32 µm). However, the CC specimens show lower S_z compared to L-PBF1-G (−33.19 µm) and L-PBF1-M (−2.15 µm), respectively, which is less pronounced for milled condition, Table 4.

Comparing the subtractive manufacturing processes used, higher S_a and S_z were observed for ground compared to milled specimens for all variants, Table 4.

In addition to the surface topography, the residual stresses resulting from finishing were measured for CC and L-PBF2 specimens, *Figure 7*. Because of the high porosity of L-PBF1 specimens, a reliable measurement of the process-induced residual stresses was not possible. For L-PBF2 specimens only small residual tensile stresses can be observed, which are similar for both finishing processes and hence, should not significantly influence the mechanical properties, Figure 7. In contrast to that, the ground CC specimens show significantly higher residual tensile stresses compared to CC–M specimens (about 150 MPa). Moreover, the CC specimens reveal more pronounced residual

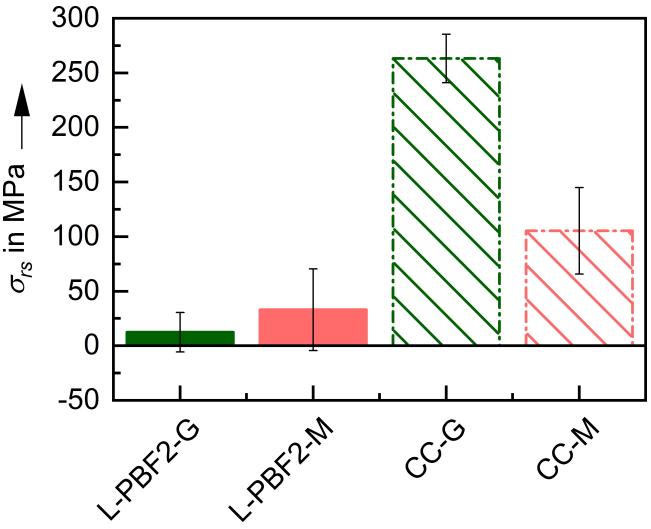

Figure 7. Surface near residual stresses σ_{rs} in loading direction of L-PBF2 and CC specimens resulting from subtractive finishing.

Bild 7. Aus den unterschiedlichen Oberflächennachbearbeitungen resultierende Oberflächeneigenspannungen σ_{rs} in Beanspruchungsrichtung der L-PBF2 und CC-Proben.

stresses than the L-PBF2 specimens, Figure 7. Considering this and the observed surface topographies, the finishing processes lead to substantially different surface morphology for continuously cast compared to additively manufactured material. The different surface morphologies obtained for CC compared to L-PBF2 specimens indicates a difference in the interrelation between subtractive manufacturing and process-related microstructure. The impact of these differences in surface condition on the fatigue behavior is discussed in detail in section 4.3.[1]

4 Results and discussion

4.1 Influence of the additive manufacturing process parameters on the fatigue behavior

In this chapter the influence of the laser-based powder bed fusion process parameters on the fatigue behavior is discussed, while the influence of subtractive manufacturing and the resulting surface condition is described in detail in section 4.3. Note that the obtained fatigue data in the present work is limited for each condition and hence, can only be used as a rough approximation of the *S-N*$_f$ curves, *Figure 8*. However, the observed scatter is comparably small for all variants and consequently, the presented results are sufficient to qualitatively analyze the fatigue behavior and its dependency on the manufacturing process.

Comparing the *S-N*$_f$ curves obtained from the L-PBF1 and L-PBF2 specimens, the parameter set L-PBF2 yields a massively higher fatigue strength for all surface conditions, Figure 8. This corresponds to the significantly lower porosity and smaller defect sizes achieved with L-PBF2, Table 3. Moreover, the L-PBF2 specimens show a smaller S_z in all surface conditions, which also contributes to the higher fatigue strength, Table 4. However, the difference in porosity between L-PBF1 and L-PBF2

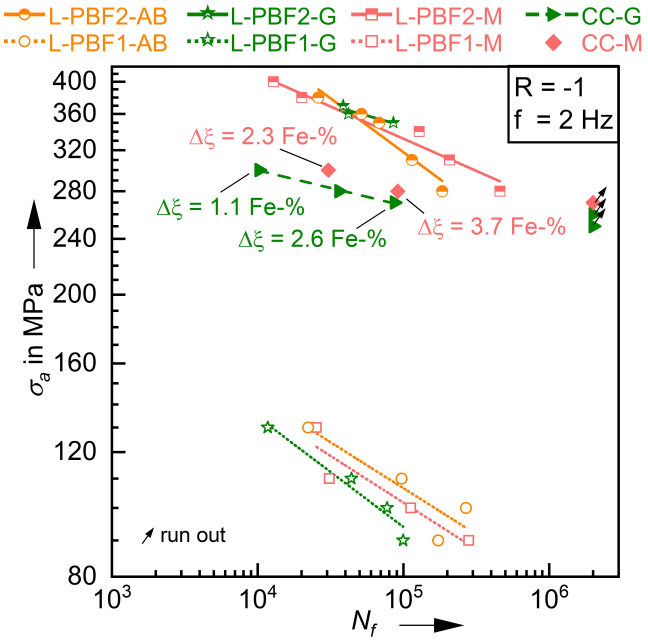

Figure 8. Comparison of the fatigue lifetime data as well as the resulting *S-N*$_f$ curves of the differently manufactured specimens with different surface morphologies as well as increase of magnetic fraction $\Delta\zeta$ for continuously cast specimens.

Bild 8. Vergleich der Ermüdungslebensdauern sowie der resultierenden Wöhlerkurven für die verschieden hergestellten, unterschiedliche Oberflächenmorphologien aufweisenden, Ermüdungsproben sowie das Ausmaß des Anstiegs des magnetischen Phasenanteils $\Delta\zeta$ der stranggegossenen Proben.

[1] Naming of specific manufacturers is done solely for the sake of completeness and does not necessarily imply an endorsement of the named companies nor that the products are necessarily the bests for the purpose.

specimens is significantly more pronounced than the difference in surface roughness. Consequently, it is assumed that the extensively lower fatigue strength of L-PBF1 specimens is mainly caused by the higher porosity, Table 3. This assumption is confirmed by the fatigue fracture surfaces, revealing only crack initiation at process-induced microstructural defects, i. e., pores and lack of fusion, at the "as-built", ground or milled surface, Figures 1, *9*. These defects are significantly larger and are connected within the fracture surfaces in the L-PBF1 specimens, resulting in a substantially greater notch effect and thus, in a more extended stress intensity, which leads to a significant reduction of fatigue strength.

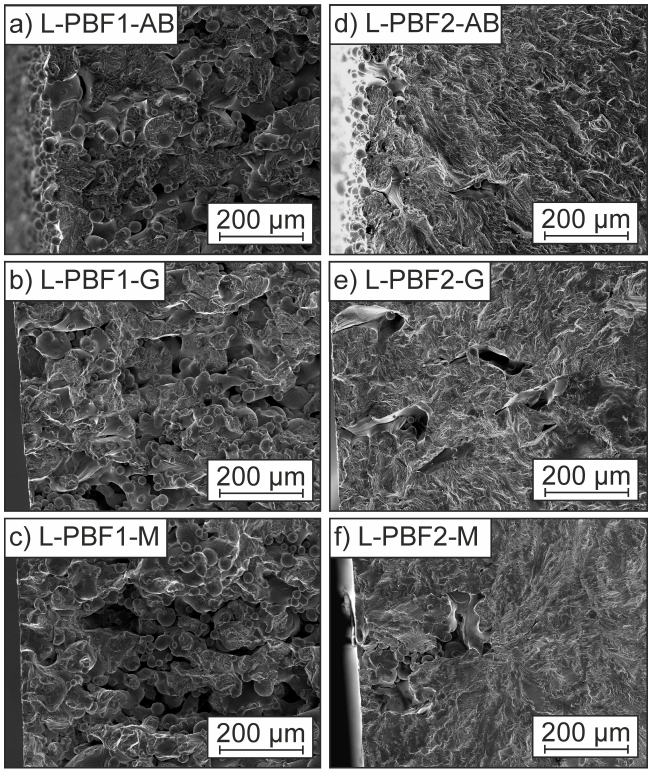

Figure 9. Fatigue fracture surfaces for a) L-PBF1-AB ($\sigma_a = 110$ MPa; $N_f = 96{,}965$), b) L-PBF1-G ($\sigma_a = 100$ MPa; $N_f = 77{,}258$), c) L-PBF1-M ($\sigma_a = 110$ MPa; $N_f = 30{,}976$), d) L-PBF2-AB ($\sigma_a = 360$ MPa; $N_f = 51{,}644$), e) L-PBF2-G ($\sigma_a = 370$ MPa; $N_f = 38{,}664$) and f) L-PBF2-M ($\sigma_a = 280$ MPa; $N_f = 459{,}675$).

Bild 9. Ermüdungsbruchflächen von a) L-PBF1-AB ($\sigma_a = 110$ MPa; $N_f = 96.965$), b) L-PBF1-G ($\sigma_a = 100$ MPa; $N_f = 77.258$), c) L-PBF1-M ($\sigma_a = 110$ MPa; $N_f = 30.976$), d) L-PBF2-AB ($\sigma_a = 360$ MPa; $N_f = 51.644$), e) L-PBF2-G ($\sigma_a = 370$ MPa; $N_f = 38.664$) und f) L-PBF2-M ($\sigma_a = 280$ MPa; $N_f = 459.675$).

For specimens manufactured with both parameter sets, multiple crack initiation can be observed, resulting from a great number of process-induced defects located at the surface, which show different morphologies. Note that for each condition different kinds of defect morphologies led to fatigue crack initiation and no influence of defect morphology on fatigue lifetime was observed. However, the number of crack initiation sites is substantially higher for L-PBF1 compared to L-PBF2 specimens in all surface conditions, which results from the bigger size and larger number of process-induced defects of this condition. Note that for L-PBF2-M only at $\sigma_a = 400$ MPa multiple crack initiation was observed, whereas at lower stress amplitudes the crack was initiated at one big process-induced defect for this condition, Figure 9f.

In addition to the fatigue lifetime and the fracture surfaces, the cyclic deformation behavior of the differently manufactured materials was analyzed. The cyclic deformation curves obtained in fatigue tests at L-PBF1 specimens reveal a significantly lower amount of plastic strain amplitude $\varepsilon_{a,p}$ compared to the curves from L-PBF2 specimens, *Figure 10*a, b. Furthermore, the specimens from both parameter sets only show cyclic softening during the fatigue tests, which is in correspondence to preliminary results and is more pronounced for L-PBF2 specimens [19–22]. The higher level of plastic deformation and stronger cyclic softening is caused by higher stress amplitudes σ_a used in fatigue tests with L-PBF2 specimens, Figure 10 a, b. However, it has to be considered that the different stress amplitudes led to comparable fatigue lifetimes, which underlines the significant differences in fatigue behavior between L-PBF1 and L-PBF2 specimens.

Although the significantly lower fatigue strength of L-PBF1 is not surprising, the present results demonstrate a high influence of process-induced defects, and thus, of manufacturing parameters used in laser-based powder bed fusion on the fatigue behavior of additively manufactured materials.

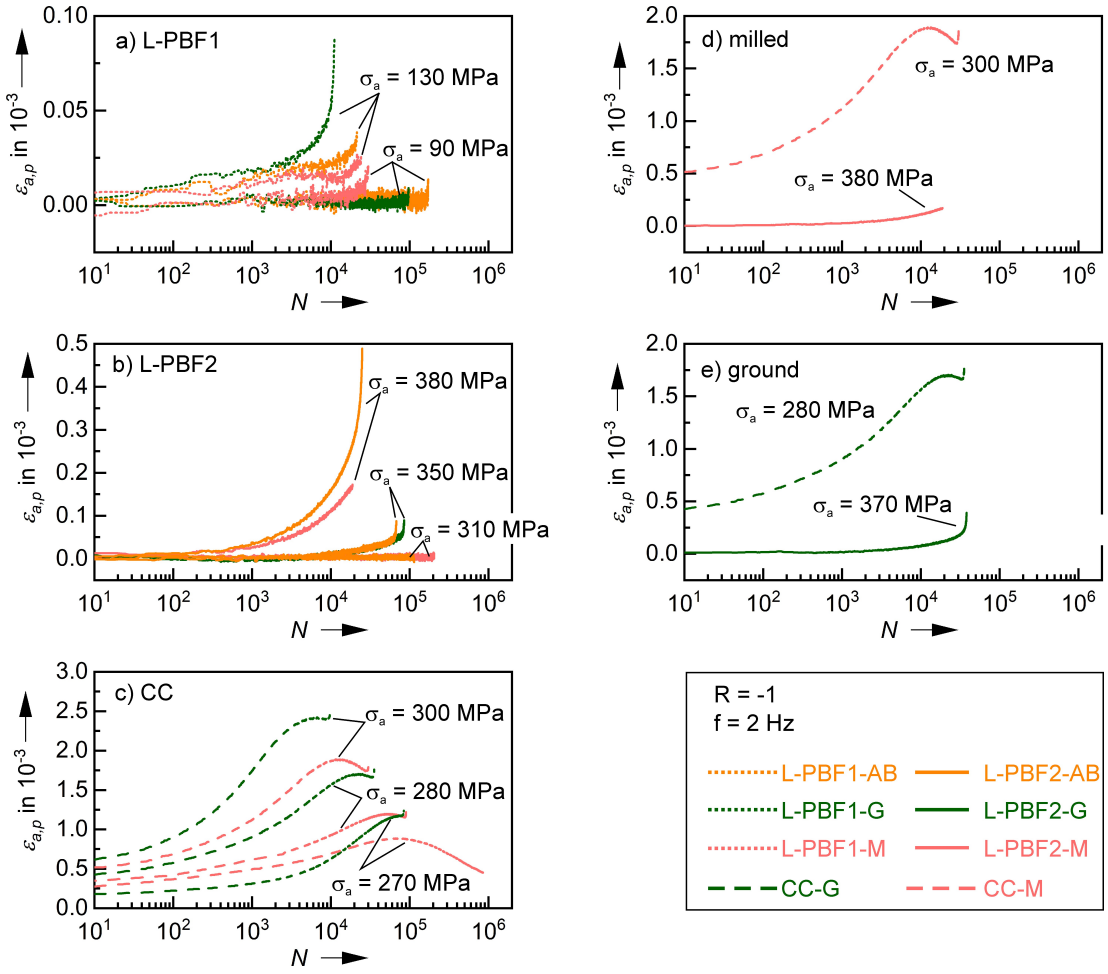

Figure 10. Cyclic deformation curves (evolution of plastic strain amplitude $\varepsilon_{a,p}$) obtained in fatigue tests with the differently manufactured specimens, including the stress amplitudes σ_a applied.

Bild 10. In Ermüdungsversuchen ermittelte Wechselverformungskurven (Veränderung der plastischen Dehnungsamplitude $\varepsilon_{a,p}$) der unterschiedlich hergestellten Proben sowie der Angabe der jeweiligen Spannungsamplitude σ_a.

4.2 Comparison of the fatigue behavior of additively (L-PBF2) and conventionally manufactured specimens

As L-PBF1 represents an inadequate process parameter set and it yields dramatically lower fatigue strength, in this chapter only L-PBF-2 specimens are compared to continuously cast material. The influence of subtractive manufacturing process is discussed in detail in section 4.3.

In comparison to L-PBF2, the CC specimens show a significantly lower fatigue lifetime at higher stress amplitudes ($\sigma_a \geq 300$ MPa) for both machined surface conditions, while more similar number of cycles to failure N_f can be observed at lower stress amplitudes ($\sigma_a < 280$ MPa), Figure 8.

The longer fatigue lifetimes at higher stresses can be explained by the higher strength of the additively manufactured material volume, which is indicated by the higher hardness, Table 3. Moreover, the cyclic deformation curves reveal more pronounced plastic deformation (higher $\varepsilon_{a,p}$) for CC specimens, even at lower stress amplitudes σ_a, compared to L-PBF2 specimens, Figure 10d, e. This also indicates a higher strength of the additively manufactured material volume. The longer fatigue lifetime of L-PBF2 specimens in this stress regime is independent of the surface condition and can also be observed for "as-built" specimens with relatively high S_z. Consequently, the surface roughness seems to be a minor influencing factor on the fatigue behavior at higher stresses.

Because of an increasing influence of microstructural notches with decreasing load amplitudes, the process-induced defects have to be taken into account by analyzing the differences in fatigue behavior at lower stresses. It has to be considered, that the CC specimens showed in contrast to L-PBF2 specimens no microstructural defects at crack initiation sites. At lower stress amplitudes the number of cycles to failure of L-PBF2 specimens converges to the values of defect-free CC specimens. Thus, it is assumed that at lower stress amplitudes the effect of process-induced defects becomes more important than the higher strength of the additively manufactured material volume and consequently, dominates the fatigue behavior.

Besides the impact of process-induced defects and surface-induced notch effects, the difference in austenite stability between continuously cast and additively manufactured material has to be taken into account. The magnetic fraction ζ increases in CC specimens during fatigue tests, Figure 8. This is caused by deformation-induced transformation from paramagnetic austenite to ferromagnetic α'-martensite, resulting in cyclic hardening after initial cyclic softening in the fatigue tests, which can only be seen in the cyclic deformation curves of CC specimens, Figure 10c–e. This deformation-induced α'-martensite formation increases the fatigue lifetime at stress-controlled fatigue tests [19, 20, 41]. Furthermore, an increasing amount of phase transformation with decreasing stress amplitude can be observed, Figure 8. Consequently, also the phase transformation contributes to flatter S-N_f curves of continuously cast specimens in relation to the additively manufactured material. However, the increasing influence of process-induced defects seems to be the main reason for the more similar fatigue lifetime of the CC and L-PBF2 specimens at lower stress amplitudes.

When comparing the fatigue behavior of CC and L-PBF2 specimens, also the influence of residual stresses has to be considered. For similar finishing processes one may expect a shorter fatigue lifetime for CC specimens caused by the relatively high residual tensile stresses, Figure 7. However, the amount of plastic deformation observed in fatigue tests of the CC specimens is relatively high and consequently, the influence of residual stresses on the fatigue lifetime are supposed to be neglectable due to relaxation processes [42]. Because relaxation effects are less pronounced with decreasing stress amplitude and thus, smaller plastic strain amplitude $\varepsilon_{a,\,p}$, a residual stress-induced reduction of fatigue lifetime for CC specimens should be more pronounced at smaller stresses. In contrast to that, the S-N_f curves show converging fatigue lifetime for CC and L-PBF2 specimens with decreasing stress amplitudes, which underlines the neglectable influence of the measured residual stresses, Figure 8.

Finally, it is worth mentioning that despite pronounced process-induced microstructural defects, the fatigue strength of machined L-PBF2 specimens is comparable to conventionally manufactured material.

4.3 Influence of the subtractive manufacturing process on the fatigue behavior of the differently manufactured materials

For understanding the influence of subtractive finishing on the fatigue behavior, first the CC–M and CC–G specimens are compared. The ground specimens show a higher level of plastic deformation, leading to significantly shorter fatigue lifetimes, Figure 10c. Moreover, grinding resulted in a slightly higher surface roughness than milling, which also contributes to lower number of cycles to failure of CC–G specimens, Table 4.

As discussed in detail in section 4.2, the influence of residual stresses on the fatigue behavior is assumed to be neglectable for the presented investigations, because of the relatively high amount of plastic deformation in the fatigue tests, Figure 10c–e. Consequently, the higher residual tensile stresses of CC–G compared to CC–M specimens are assumed to not significantly impact the fatigue behavior. However, as already discussed in section 3.2, the different residual tensile stresses indicate differences in surface morphology between the milled and ground condition of CC specimens, which is in accordance with [33, 43] and has to be considered. Exemplarily, differently pronounced nanocrystalline surface layers were observed for different finishing processes, which is also expected for the materials investigated in this work and is objective of further investigations [33]. Nevertheless, the presented results of continuously cast material demonstrate that the subtractive finishing processes

applied lead to significant differences in the fatigue behavior of CC specimens.

Despite the significantly different S_a and S_z, the S-N_f curves of the L-PBF1 specimens reveal comparable fatigue lifetimes in the HCF-regime for all surface conditions, Table 4, Figure 8. Although the L-PBF1-AB specimens exhibit a massively higher surface roughness than the machined specimens, the "as-built" condition generally has higher fatigue lifetimes. However, considering the relatively small number of fatigue tests, the differences in S-N_f curves seem to be within the lifetime scatter of the different surface conditions. Furthermore, the cyclic deformation curves are nearly identical for all conditions, Figure 10a. Thus, no substantial influence of subtractive manufacturing on the fatigue behavior of the material produced with L-PBF1 can be observed.

By comparing the fatigue fracture surfaces of different L-PBF1 specimens, crack initiation at process-induced defects, which are comparable for all surface conditions, can be observed, Figure 9a–c. Because the sizes of the process-induced defects are bigger than the height of the surface roughness peaks, the influence of the surface roughness is neglectable and the microstructural notch effect from process-induced defects is assumed to be dominant. Therefore, no measurable influence of surface finishing on fatigue lifetime can be observed.

At high stress amplitudes ($\sigma_a \geq 340$ MPa), also for the L-PBF2 specimens similar fatigue lifetimes were observed for the three surface conditions "as-built", ground and milled. Additionally, the cyclic deformation curves obtained in the fatigue tests are nearly identical, which is in contrast to the results obtained with CC specimens, Figure 10b, c. With regard to the significant differences in surface roughness between L-PBF2-AB, L-PBF2-G and L-PBF2-M, Table 4, these results are surprising. However, the fatigue cracks in the L-PBF2 specimens are initiated at process-induced defects, Figure 9d–f. This is similar to the results of L-PBF1, whereby the difference between the height of the surface roughness peaks and the size of the defects is less pronounced for L-PBF2 specimens.

At lower stress amplitudes ($\sigma_a \leq 300$ MPa) L-PBF2-AB, which has significantly higher S_a and S_z than L-PBF2-G or L-PBF2-M, reveals slightly shorter fatigue lifetime. The influence of surface topography increases with decreasing stress amplitudes and thus, only leads to shortened fatigue lifetime in this stress regime (comp. [21]). Note that also for L-PBF2 specimens only limited data is available and hence, only a qualitative analysis is possible. In summary, an influence of surface finishing on fatigue lifetime can be observed only at low stress amplitudes. However, the differences between milled and ground condition is less pronounced compared to CC material, which is assumed to be caused by the high influence of process-induced defects.

For a decreasing level of porosity combined with smaller defects, an increasing influence of surface machining on the fatigue behavior is expected. Subsequent machining and polishing of additively manufactured specimens with small process-induced pores result in substantially higher fatigue strength [21]. Although the porosity of L-PBF2 is significantly lower compared to L-PBF1 specimens, the size and number of defects observed in L-PBF2 specimens are big in relation to the specimens examined, resulting in a less pronounced difference in fatigue behavior of finished and "as-built" specimens [21].

The presented results reveal that subtractive manufacturing processes lead to different surface roughness, residual stresses and fatigue behavior for additively manufactured material compared to conventionally manufactured material. This can be explained by process-related microstructures, resulting in significantly different surface morphologies for CC specimens and L-PBF specimens after subtractive manufacturing, which is objective of future work. Moreover, the presented results demonstrate that the degree of improvement of the fatigue strength of additively manufactured structures by a subsequent machining is dependent on the size as well as number of process-induced defects in the material volume. Consequently, a laser-based powder bed fusion process resulting in a high density of the material is the basis for a long fatigue lifetime of highly loaded components. However, for structures with high porosity a post surface machining can be considered as obsolete with regard to the fatigue performance.

5 Summary and conclusion

In this work, the fatigue behavior of "additively-subtractively" manufactured specimens, which are defined as additively manufactured and subsequently machined specimens, made of austenitic stainless steel AISI 316L was characterized. Therefore, fatigue specimens were manufactured with laser-based powder bed fusion (L-PBF) by using two process parameter sets, leading to significantly different porosity as well as surface roughness. Specimens with "as-built" (AB), ground (G) and milled (M) surface conditions were investigated. Moreover, continuously cast (CC) material with ground and milled surfaces served as reference for conventional manufacturing. For analyzing the cyclic deformation behavior, the influence of surface roughness as well as process-induced defects, i. e., pores and lack of fusion, were considered. Furthermore, the deformation-induced austenite-α'-martensite transformation was taken into account and was only observed at CC specimens, because of their substantially lower austenite stability. This phase transformation leads to a beneficial effect on the fatigue lifetime of the CC specimens in the high cycle fatigue regime.

The comparison of the fatigue lifetimes, the cyclic deformation behavior and the fatigue fracture surfaces obtained in fatigue tests, combined with microstructural and surface topography analyses, lead to the following conclusions:

- The subtractive manufacturing processes lead to a significantly lower surface roughness of additively manufactured specimens, which is comparable or even smaller in relation to the results obtained at continuously cast specimens. For the examined parameter sets, a smaller surface roughness was achieved by using milling compared to pendulum grinding.
- The process parameters used for laser-based powder bed fusion significantly influence the surface roughness and especially the porosity of the specimens. The parameter set with significantly lower volume energy density led to a dramatically higher porosity and extensively bigger defects, i. e. pores and lack of fusion, resulting in significantly reduced fatigue strength.
- The fatigue lifetime of "additively-subtractively" manufactured specimens is mainly dependent on the defects resulting from additive manufacturing and hence, the subtractive manufacturing processes show less pronounced influence on the fatigue lifetime compared to continuously cast specimens. For continuously cast specimens a higher fatigue lifetime could be observed for the milled than for the ground condition.
- Comparing continuously cast and additively manufactured specimens, significant differences regarding surface roughness and residual stresses could be observed after finishing. Consequently, the effects of subtractive finishing vary between conventionally and additively manufactured materials, which is caused by the substantially different microstructures.
- The impact of finishing of additively manufactured structures on fatigue behavior is dependent on the size and distribution of process-induced defects, which is influenced by the parameters used for additive manufacturing. Thus, process parameters that lead to a high density and small process-induced defects are a prerequisite for the production of highly loaded, safety relevant components.

Finally, the presented results demonstrate complex interrelations between additive and subtractive manufacturing processes, which will be investigated in future research. These activities will be focused on materials with less porosity and smaller defects, including thorough analysis of the surface morphology caused by additive-subtractive manufacturing.

Acknowledgements

The financial support of the priority research activity of Rhineland Palatinate "Advanced Materials Engineering (AME)" is gratefully acknowledged. We further thank Prof. J. Seewig that we were allowed to perform the confocal microscopy investigations at the Institute for Measurement and Sensor-Technology of TU Kaiserslautern. Open Access funding enabled and organized by Projekt DEAL.

6 References

[1] A. Riveiro, J. del Val, R. Comesaña, F. Lusquiños, F. Quintero, M. Boutinguiza, J. Pou,

Near Net Shape Manufacturing Processes **2019**, 105.
[2] R. Kleer, F.T. Piller, *Int. J. Production Economics* **2019**, *216*, 23.
[3] M. Islam, T. Purtonen, H. Piili, A. Salminen, O. Nyrhilä, *Phys. Procedia* **2013**, *41*, 835.
[4] B. Nagarajan, Z. Hu, X. Song, W. Zhai, J. Wei, *Engineering* **2019**, *5*, 702.
[5] E. Yasa, J-P. Kruth, *Procedia Eng.* **2011**, *19*, 389.
[6] T.M. Mower, M.J. Long, *Mater. Sci. Eng. A* **2016**, *651*, 198.
[7] A. Riemer, S. Leuders, M. Thöne, H.A. Richard, T. Tröster, T. Niendorf, *Eng. Fract. Mech.* **2014**, *120*, 15.
[8] T. Bauer, K. Dawson, A.B. Spierings, K. Wegener, presented at *26th Annual International Solid Freeform Fabrication Symposium*, Austin, Texas, 10 August – 12 August, **2015**, pp. 813–822.
[9] L. Liu, Q. Ding, Y. Zhong, J. Zou, J. Wu, Y.-L. Chiu, J. Li, Z. Zhang, Q. Yu, Z. Shen, *Mater. Today* **2018**, *21*, 354.
[10] R. Rai, J.W. Elmer, T.A. Palmer, T. DebRoy, *J. Phys. D Appl. Phys.* **2007**, *40*, 5753.
[11] J.A. Cherry, H.M. Davies, S. Mehmood, N.P. Lavery, S.G.R. Brown, J. Sienz, *Int. J. Adv. Manuf. Technol.* **2015**, *76*, 869.
[12] H. Gu, H. Gong, D. Pal, K. Rafi, T. Starr, B. Stucker, presented at *24th Annual International Solid Freeform Fabrication (SFF) Symposium*, Austin, Texas, 12 August – 14 August, **2013**, pp. 474–489.
[13] E. Abele, H.A. Stoffregen, M. Kniepkamp, S. Lang, M. Hampe, *J. Mater. Process. Technol.* **2015**, *215*, 114.
[14] P. Edwards, M. Ramulu, *Mater. Sci. Eng. A* **2014**, *598*, 327.
[15] A. Ahmed, A. Majeed, Z. Atta, G. Jia, *Journal of Manufacturing and Materials Processing* **2019**, *3*, 51.
[16] J. Delgado, J. Ciurana, C.A. Rodríguez, *Int. J. Adv. Manuf. Tech.* **2012**, *60*, 601.
[17] A. Yadollahi, N. Shamsaei, S.M. Thompson, A. Elwany, L. Bian, *Int. J. Fat.* **2017**, *94*, 218.
[18] S. Leuders, M. Thöne, A. Riemer, T. Niendorf, T. Tröster, H.A. Richard, H.J. Maier, *Int. J. Fat.* **2013**, *48*, 300.
[19] B. Blinn, M. Klein, C. Gläßner, M. Smaga, J.C. Aurich, T. Beck, *Metal* **2018**, *8*, 220.
[20] B. Blinn, F. Krebs, M. Ley, C. Gläßner, M. Smaga, J.C. Aurich, R. Teutsch, T. Beck, *Metals* **2019**, *9*, 1285.
[21] B. Blinn, F. Krebs, M. Ley, R. Teutsch, T. Beck, *Int. J. Fat.* **2020**, *131*, 105301.
[22] B. Blinn, M. Ley, N. Buschhorn, R. Teutsch, T. Beck, *Int. J. Fat.* **2019**, *124*, 389.
[23] A.B. Spierings, G. Levy, presented at *20th Annual International Solid Freeform Fabrication (SFF) Symposium*, Austin, Texas, 3 August – 5 August, **2009**, pp. 342–353.
[24] M.P. Sealy, G. Madireddy, R.E. Williams, P. Rao, M. Toursangsaraki, *J. Manuf. Sci. Eng.* **2018**, *140*, 79.
[25] T. Grove, B. Denkena, O. Maiß, A. Krödel, H. Schwab, U. Kühn, *Journal of Mechanical Science and Technology* **2018**, *32*, 4883.
[26] J.C. Aurich, S. Greco, H. Hotz, M. Zimmermann, J. Hartig, B. Kirsch, *ZWF* **2017**, *112*, 473.
[27] J.C. Aurich, F. Schneider, B. Kirsch, M. Zimmermann, *ZWF* **2017**, *112*, 465.
[28] P. Mercelis, J.-P. Kruth, *Rapid Prototyp. J.* **2006**, *12*, 254.
[29] Y. Liu, Y. Yang, D. Wang, *Int. J. Adv. Manuf. Technol.* **2016**, *87*, 647.
[30] W. Du, Q. Bai, B. Zhang, *Int. J. Adv. Manuf. Tech.* **2018**, *95*, 2509.
[31] Y. Kaynak, O. Kitay, *Addit. Manuf.* **2019**, *26*, 84.
[32] B. Breidenstein, F. Brenne, L. Wu, T. Niendorf, B. Denkena, *HTM* **2018**, *73*, 173.
[33] M. Smaga, R. Skorupski, P. Mayer, B. Kirsch, J.C. Aurich, I. Raid, J. Seewig, J. Man, D. Eifler, T. Beck, *Procedia Structural Integrity* **2017**, *5*, 989.
[34] A. Boemke, M. Smaga, T. Beck, presented at *Fatigue*, Portiers, France, 27 May – 1 June, **2018**, pp. 165.
[35] S. Greco, K. Gutzeit, H. Hotz, B. Kirsch, J.C. Aurich, *Int. J. Adv. Manuf. Technol.* **2020**, *108*, 1551.
[36] N.A. Riley, *J. Sediment. Res.* **1941**, *11*, 94.
[37] DIN EN ISO 25178-2, German version, Beuth, Berlin, September **2012**.

[38] ASTM A 240/ A 240Ma, Information Handling Services, West Conshohocken, Pennsylvania, USA, December **2016**.
[39] T. Angel, *Journal of the Iron and Steel Institute* **1954**, *177*, 165.
[40] D. Novovic, R.C. Dewes, D.K. Aspinwall, W. Voice, P. Bowen, *Int. J. Mach. Tools Manuf.* **2004**, *44*, 125.
[41] M. Smaga, F. Hahnenberger, A. Sorich, D. Eifler, *Key Eng. Mater.* **2011**, *465*, 439.
[42] I. Nikitin, M. Besel, *Mater. Sci. Eng. A* **2008**, *491*, 297.
[43] M. Smaga, R. Skorupski, D. Eifler, T. Beck, *J. Mater. Res.* **2017**, *32*, 4452.

Received in final form: March 9th 2021

